NANO LETTERS

pubs.acs.org/NanoLett Letter

Surface-Charge-Regulated MoS_2 Membrane for Induced Agglomeration and Efficient Removal of Nanopollutants

Weikang Zheng,† Qutong Yang,† Mingzi Sun,† Honglu Hu, Yue Zhang, Ruixin Yan, Yang Zhou, Jingyun Fang, Alicia Kyoungjin An, Chuyang Y. Tang, Zhiguo Yuan, Kenneth M. Y. Leung, Bolong Huang,* and Zhiyuan Zeng*

Cite This: https://doi.org/10.1021/acs.nanolett.6c02107 Read Online

ACCESS | Metrics & More | Article Recommendations | Supporting Information

ABSTRACT: Conventional membranes for nanopollutant removal are constrained by the permeability−selectivity trade-off inherent in size-exclusion mechanisms. Here, we report a surface-charge-regulated MoS_2 membrane engineered by anchoring copper nanoparticles and quaternary ammonium groups onto MoS_2 nanosheets. This functionalization creates a porous 3D architecture while tuning the surface charge density to induce the agglomeration of oppositely charged nanopollutants (e.g., nanoplastics and metal oxides), effectively increasing their size for enhanced rejection. The optimized copper-functionalized membrane (M-I-Cu0.63) achieves an exceptional water permeance of 804.3 ± 35.4 L/(m^2·h·bar) with 99.68% rejection of positively charged pollutants. Conversely, the cetyltrimethylammonium bromide-functionalized counterpart (M-I-C2.4) provides a water permeance of 512.9 ± 21.1 L/(m^2·h·bar) and 99.43% rejection for negatively charged species. This charge-directed strategy overcomes intrinsic filtration limits, offering a promising route for high-efficiency, next-generation water purification.

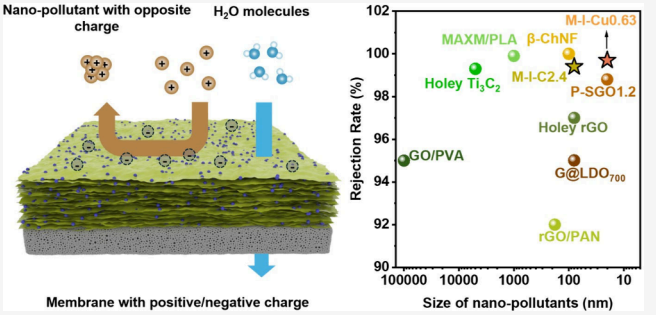

KEYWORDS: *molybdenum disulfide, surface-charge regulation, permeability−selectivity trade-off, water purification, high rejection rate*

Severe global water pollution, stemming from industrial discharges and the overuse of plastic products, has sparked heightened concerns over clean water availability.[1−4] Nanopollutants, such as nanoplastics [polystyrene (PS) and polyethylene][5−7] and metal oxide nanoparticles (TiO_2, Fe_2O_3, and ZnO),[8,9] have attracted wide attention due to their high stability, ecotoxicity, and human neurotoxicity and facile penetration of biological barriers.[10,11] Among various water purification technologies, membrane-based separation has become an essential approach, valued for its high efficiency, energy savings, and operational simplicity.[12−15] However, conventional commercial membranes often struggle to effectively reject nanopollutants and are susceptible to fouling and clogging during filtration.[16−18] Consequently, the rational design of advanced filtration membranes has become a paramount priority for addressing this pressing environmental challenge.

In recent years, two-dimensional (2D) layered nanomaterials—such as graphene,[19,20] MXenes,[21,22] and molybdenum disulfide (MoS_2)[23−26]—have emerged as promising building blocks for high-performance filtration membranes. Among these materials, MoS_2, a representative transition-metal dichalcogenide (TMD) material, stands out due to its superior chemical stability and resistance to interlayer swelling compared to other 2D materials.[27−29] Nevertheless, MoS_2-based membranes still face challenges in achieving both high water permeance and a strong rejection rate for nanopollutants. The dense stacking of nanosheets often restricts water permeability because the rejection performance for nanoscale contaminants tends to decline as flux increases, highlighting a typical permeability−selectivity trade-off.[30−32] Therefore, innovative strategies to balance water permeability and contaminant rejection are urgently required to advance the practical application of MoS_2 membranes in next-generation water-treatment technologies.

Herein, we report a straightforward strategy that combines lithium intercalation-based exfoliation with surface functionalization to introduce copper nanoparticles (Cu NPs) and quaternary ammonium groups onto 2D MoS_2 nanosheets (NSs). The functionalization strategy not only creates a more disordered porous architecture in the resulting filtration-assembled membrane but also effectively promotes the

Received: April 30, 2026
Revised: August 10, 2026
Accepted: August 13, 2026

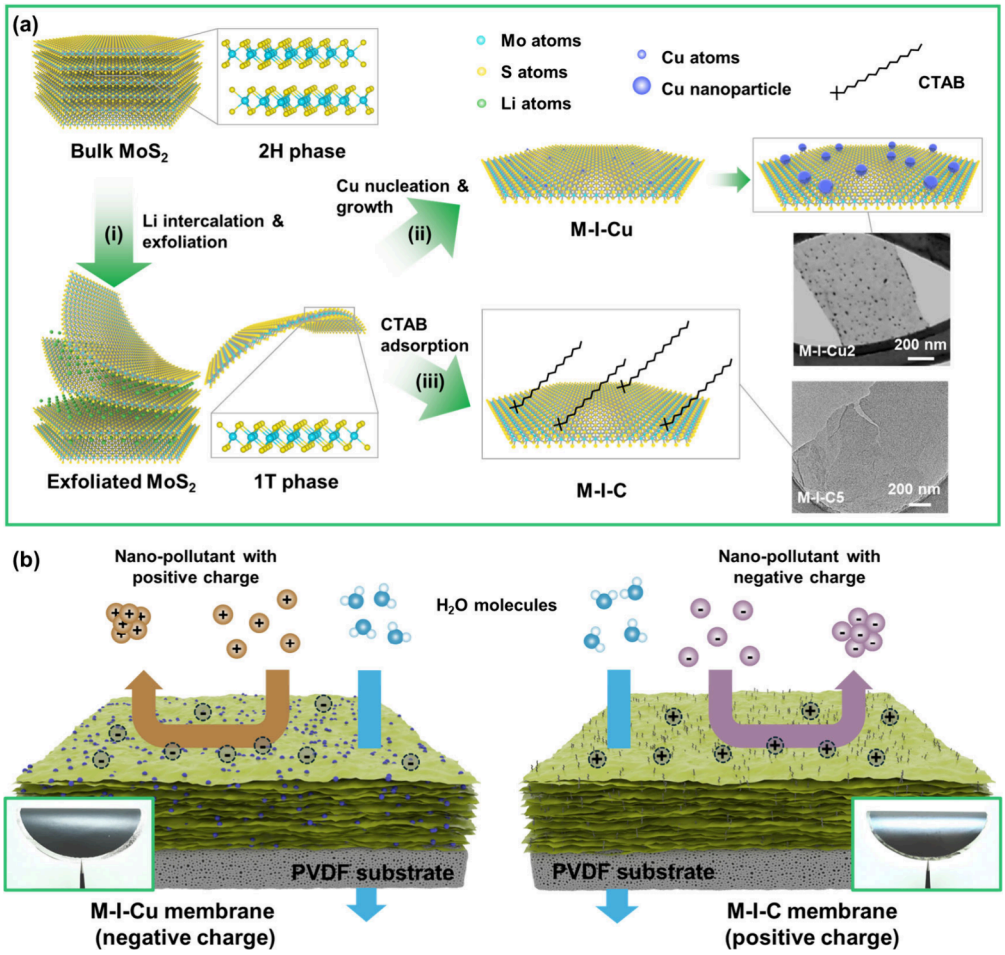

Figure 1. (a) Schematic diagram showing the preparation and functionalization process of MoS_2 NSs. Inset images are the TEM images of MoS_2 NSs functionalized by 2 mM $Cu(OAc)_2$ and 5 mM CTAB. (b) Rejection mechanism of positively/negatively charged nanopollutants by MoS_2 membranes functionalized by $Cu(OAc)_2$ and CTAB. Inset images are the digital photographs of the corresponding bent membranes.

agglomeration of oppositely charged nanopollutants. This innovative structural and chemical optimization successfully overcomes the intrinsic permeance−rejection trade-off that commonly existed in conventional separation membranes. This work presents an effective strategy for designing and fabricating next-generation MoS_2-based nanofiltration membranes with high permeability (>500 $L/m^2 \cdot h \cdot bar$), high rejection rate (>99%), and excellent stability (the performance remains unchanged after 10 cycles) for advanced water purification.

The building units of the modified MoS_2 membrane were fabricated by following the schematic diagram shown in Figure 1a. First, a controllable electrochemical lithium-ion (Li^+) intercalation-based exfoliation strategy was employed to prepare monolayered MoS_2 NSs.[33−36] By setting the cutoff voltage to 0.9 V, Li^+ ions uniformly inserted into the interlayers of bulk MoS_2, inducing a phase transformation from 2H to 1T.[37−39] Subsequent reaction of the intercalated materials with water generated gas bubbles to accelerate exfoliation of MoS_2-layered materials, thereby producing single-layer MoS_2 NS.[40] Next, the MoS_2 NSs were functionalized by copper acetate [$Cu(OAc)_2$] and hexadecyltrimethylammonium bromide (CTAB) in an isopropyl alcohol (rationale shown in Figure S1) solution to regulate the surface charge. The purpose of adding $Cu(OAc)_2$ is to introduce a large number of Cu NPs onto the surface of the nanosheets, thereby enhancing the negative charge density. Similarly, the addition of CTAB attaches positively charged carbon chains to the nanosheet surfaces through electrostatic adsorption, thus introducing positive charges to the nanosheets. Such charge modification significantly influences the interaction between the nanosheets and various nanopollutants, which further enhances their performance in water purification. Finally, as illustrated in Figure 1b, the M-I-Cu/M-I-C membranes were formed through a straightforward vacuum filtration process, during which the modified nanosheets restacked to create the layered structure. All membranes were stored submerged in water before testing to prevent any structural alterations that could occur upon drying.[41] The modifiers introduced between the layers significantly enlarge the interlayer spacing during the restacking process, allowing for faster water permeation. Additionally, the charge on the nanosheets enhances the aggregation of nanopollutants with opposite charges, which effectively enhances the contaminant rejection performance.

The growth mechanism of Cu NPs on the surface of MoS_2 NSs was systematically investigated. As revealed by the transmission electron microscopy (TEM) images in Figures 2a and S2, both the size and density of the nanoparticles increase progressively with increasing $Cu(OAc)_2$ concentration. The few-layer structure of the functionalized MoS_2 NS was confirmed by two distinct sets of diffraction patterns (inset image of Figure 2a) and atomic force microscopy (AFM) images (Figure S3). The pristine exfoliated MoS_2 NSs possess

https://doi.org/10.1021/acs.nanolett.6c02107
Nano Lett. XXXX, XXX, XXX−XXX

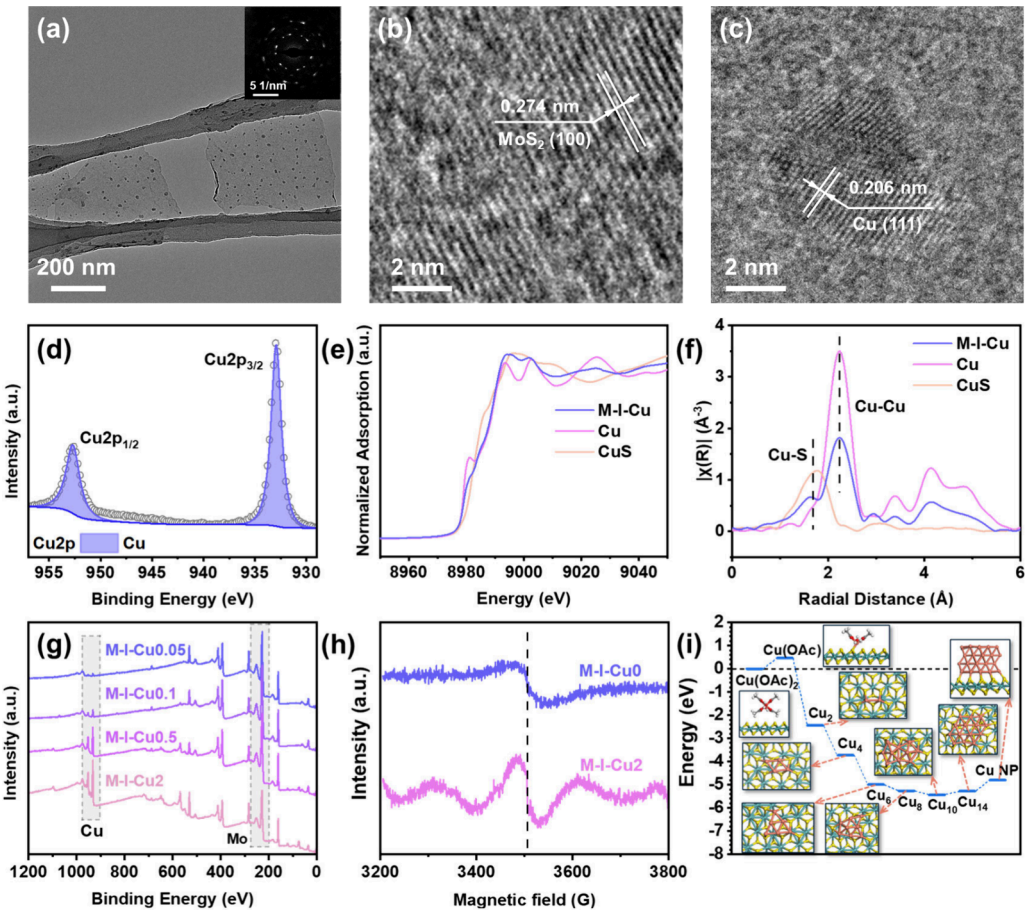

Figure 2. (a) TEM image of MoS_2 NSs functionalized by 2 mM $Cu(OAc)_2$. The inset image is the electron diffraction pattern. HRTEM images of (b) MoS_2 NS and (c) Cu NPs. (d) Cu 2p XPS spectra, (e) Cu K-edge XANES spectra, and (f) EXAFS spectra of M-I-Cu2 NSs. (g) XPS spectra of M-I-CuX [CuX = 0.05, 0.1, 0.5, and 2 mM $Cu(OAc)_2$]. (h) EPR measurements of M-I-Cu0 and M-I-Cu2. (i) Reaction trends for the reduction from Cu^{2+} to form Cu NPs on MoS_2. Insets are the structural configurations of Cu during the reduction and growth process. Balls: orange, Cu; cyan, Mo; yellow, S.

a monolayer structure with a thickness of ∼1.10 nm (Figure S3a). Upon Cu functionalization, the intensive growth of dense Cu NPs expands the topographic thickness to nearly 3-fold (∼3.50 nm), successfully driving a structural transition from a monolayer to a distinct few-layer form (Figure S3b−d). High-resolution TEM (HRTEM) images (Figure 2b,c) clearly show lattice fringes corresponding to the (100) plane of MoS_2 (2.74 Å) and the (111) plane of metallic Cu (2.06 Å), indicating the successful reduction of $Cu(OAc)_2$ to Cu(0).[42] This reduction is further corroborated by X-ray photoelectron spectroscopy (XPS) analysis of the M-I-Cu NSs (Figures 2d and S4). Consistent with these findings, Cu K-edge XANES spectra (Figure 2e) show that the absorption edge of M-I-Cu closely aligns with that of metallic Cu, confirming the dominant presence of Cu(0). The Fourier-transformed Cu K-edge EXAFS spectrum (Figure 2f) exhibits a prominent peak at 2.23 Å and a weaker peak at 1.72 Å, which are assigned to Cu−Cu and Cu−S coordination shells, respectively. This suggests that Cu atoms initially anchored to S sites on the MoS_2 surface tend to aggregate and form larger Cu NPs as the $Cu(OAc)_2$ concentration increases. Consequently, the Cu content in the M-I-Cu NSs gradually rises with increasing precursor concentration, as quantified in Figures 2g, S5, and S6. Interestingly, the modification of Cu NPs induces distortion of the nanosheet lattice (Raman spectra shown in Figure S7) and the increase of S defects.[43,44] Electron paramagnetic resonance (EPR) measurements (Figure 2h) reveal a sharp symmetric resonance centered at ∼3510 G, corresponding to a g factor of ∼2.002, which is commonly assigned to unpaired electrons localized at intrinsic S vacancies.[45] Compared with M-I-Cu0, the markedly enhanced EPR intensity of M-I-Cu2 indicates an increased concentration of S-vacancy-related paramagnetic centers after Cu deposition. In addition, the appearance of broad anisotropic resonance features at ∼3310 G ($g \approx 2.12$) and ∼3670 G ($g \approx 1.91$) suggests that metallic Cu NPs interact with S-vacancy sites, giving rise to a more anisotropic local electronic environment.[46] To elucidate the growth mechanism of Cu NPs on the surface of MoS_2 NSs, we performed density functional theory (DFT) calculations. The stepwise evolution from adsorbed Cu^{2+} precursors to mature Cu NPs was systematically examined (Figure 2i). The initial reduction step from $Cu(OAc)_2$ to Cu(OAc) ($Cu^{2+} \rightarrow Cu^{+}$) is endothermic with an energy increase of 0.46 eV. Strikingly, once this initial barrier is overcome, the subsequent nucleation and aggregation to form small Cu clusters (Cu_2 to Cu_{10}) become highly exothermic, driving a downhill energy profile that thermodynamically promotes the rapid growth of localized Cu clusters. However, as the clusters further grow and transition into mature nanoparticles (Cu NPs), the reaction curve undergoes an endothermic upward shift with an energy increase of 0.48 eV. This terminal energetic barrier effectively constrains the unconstrained bulklike agglomeration, thereby

https://doi.org/10.1021/acs.nanolett.6c02107
Nano Lett. XXXX, XXX, XXX−XXX

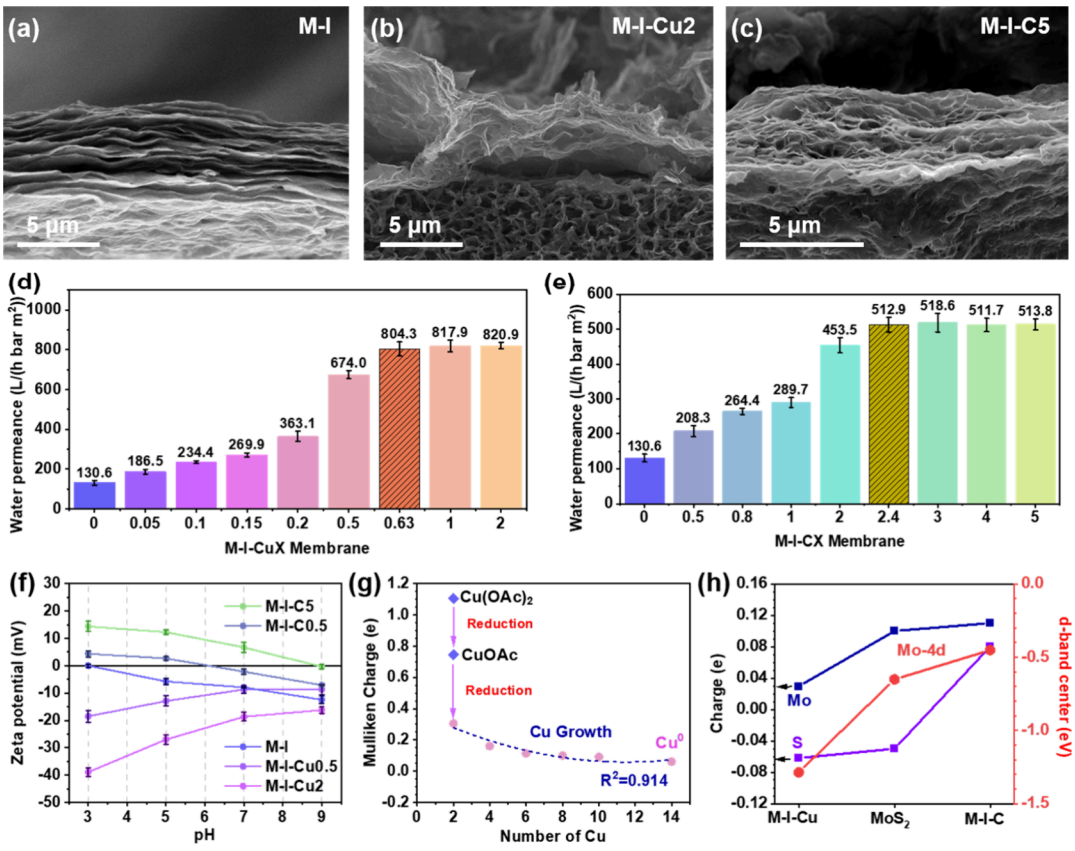

Figure 3. SEM images of (a) M-I, (b) M-I-Cu2, and (c) M-I-C5. Water permeances of (d) M-I-CuX [CuX = 0, 0.05, 0.1, 0.15, 0.2, 0.5, 0.63, 1, and 2 mM $Cu(OAc)_2$] membranes and (e) M-I-CX (CX = 0, 0.5, 0.8, 1, 2, 2.4, 3, 4, and 5 mM CTAB) membranes. (f) Surface ζ potentials of different membranes. (g) Mulliken charge evolutions of Cu sites during the reduction from Cu^{2+} to Cu^0. (h) Mulliken charges of the Mo and S sites and the Mo 4d band center before and after modification.

dictating a self-limiting size threshold for the anchored nanoparticles.

In contrast to the complex chemical growth mechanism of Cu NPs, CTAB is immobilized on the surface of MoS_2 NSs through physical interactions, which are primarily driven by hydrophobic forces and electrostatic adsorption. As shown in the TEM images (Figure S8), this functionalization process does not significantly alter the overall morphology of the nanosheets. However, a slight increase in thickness observed in the AFM images (Figure S9), the distinct nitrogen signal detected in the XPS spectrum (Figure S10), and an emerging broad organic scattering envelope in Raman spectra (Figure S11) provide compelling evidence for the successful surface attachment of CTAB molecules onto MoS_2. Increasing the CTAB concentration progressively enhances surfactant anchoring on the nanosheets, reaching a maximum modification of 15.9 wt % as X varies from 0 to 5 mM. The impact of CTAB modification on the surface charge of the nanosheets is clearly demonstrated by ζ-potential measurements (Figure S12). With increasing CTAB concentration, the ζ potential undergoes a reversal from negative to positive, indicating effective surface-charge modulation. Consequently, the resulting membrane acquires a positive surface charge that can influence its interfacial and electrostatic properties.

Membranes were freeze-dried before scanning electron microscopy (SEM) characterization to preserve their original wet-state structure.[47−49] Compared to the pure M-I membrane (Figure 3a), the M-I-Cu membranes filtered on the poly(vinylidene fluoride) substrate exhibits a unique three-dimensional (3D) porous network (shown in Figures 3b and S13), which is attributed to the nanoparticle−nanosheet structure. The highly ordered stacking of M-I-Cu0 NSs forms a typical layered structure. Nevertheless, as the copper concentration increases, this layered arrangement becomes progressively disordered [see the X-ray diffraction (XRD) patterns in Figure S15a]. A similar structural transition is observed in the M-I-C membrane, in which an increase of the CTAB concentration leads to enhanced disorder (illustrated in Figures 3c, S14, and S15b). This distinctive network significantly enhances the water permeance of the membrane when intercepting nanopollutants. As shown in Figures 3d,e and S16, dead-end filtration was employed to measure the water permeability of functionalized membranes under an applied pressure of 1 bar. With increasing modifier concentration, the water permeances of both M-I-Cu and M-I-C membranes rise linearly until reaching a plateau. Notably, in addition to the unique network structure, the enhanced surface hydrophobicity imparted by the modifier also contributes to the improvement in water permeance (Figure S17). The maximum water permeances—achieved at $Cu(OAc)_2$ and CTAB concentrations of 0.63 and 2.4 mM, respectively—reach exceptionally high values of 804.3 ± 35.4 and 512.9 ± 21.1 $L/m^2 \cdot h \cdot bar$. These values surpass those of most polymer or inorganic membranes reported to date (Table S1). Furthermore, the functionalized membranes exhibit excellent antiswelling stability and maintain macroscopically intact structures even after 72 h of continuous immersion in deionized water (Figure S18).

https://doi.org/10.1021/acs.nanolett.6c02107
Nano Lett. XXXX, XXX, XXX−XXX

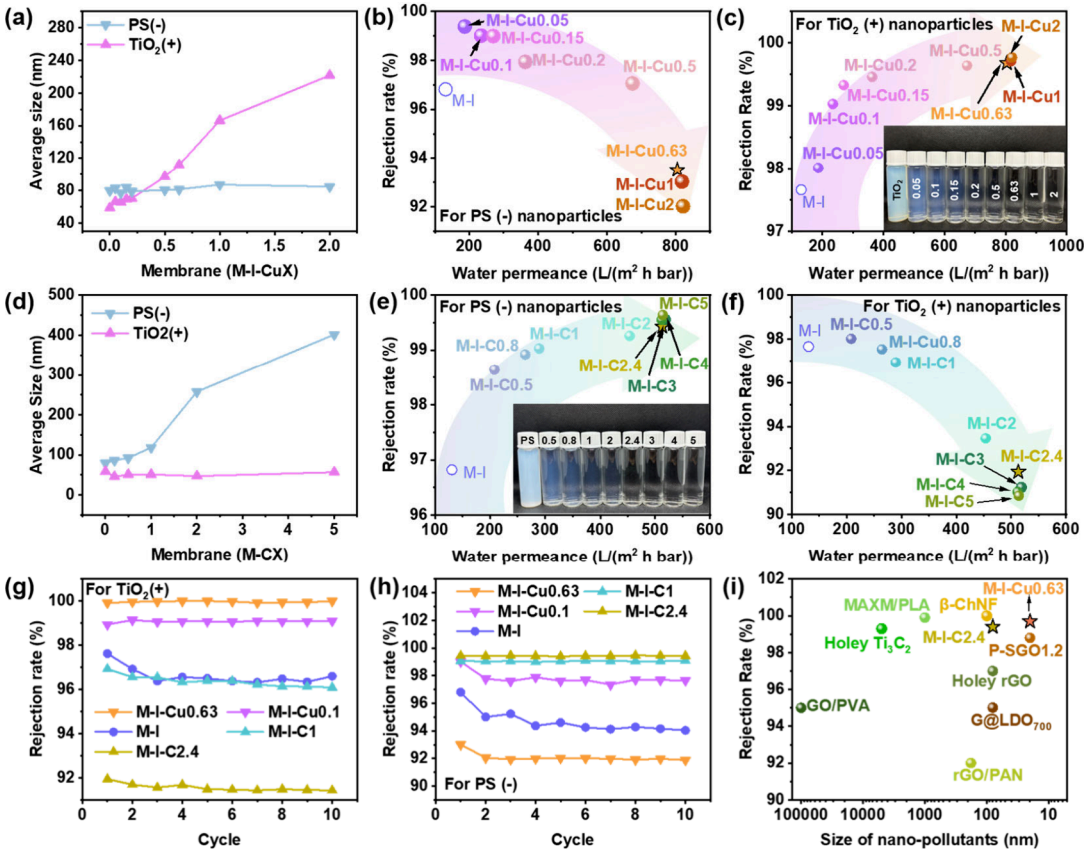

Figure 4. (a and d) Average particle size of PS and TiO_2 dispersions after immersion in M-I-CuX [CuX = 0, 0.05, 0.1, 0.15, 0.2, 0.5, 0.63, 1, and 2 mM $Cu(OAc)_2$] and M-I-CX (CX = 0, 0.5, 0.8, 1, 2, 2.4, 3, 4, and 5 mM CTAB) membranes, respectively. Water permeance and rejection performance of M-I-CuX membranes for (b) PS(−) and (c) TiO_2(+) dispersions. Water permeance and rejection of M-I-CX membranes for (e) PS(−) and (f) TiO_2(+) dispersions. The inset images in parts c and e show digital photographs of the filtrates collected using M-I-CuX [for TiO_2(+)] and M-I-CX [for PS(−)], respectively. (g and h) Cyclic stability of the functionalized membranes in TiO_2(+) and PS(−) dispersions. (i) Comparison of the water purification performance between the functionalized membranes and previously reported 2D inorganic nanosheet-based membranes.

Meanwhile, the incorporation of Cu NPs and CTAB enables effective modulation of the membrane surface charge, facilitating the agglomeration and subsequent removal of nanopollutants. Figure 3f presents the surface ζ potential of the functionalized membranes measured at various pH values. Notably, as the concentration of the modifying agent increases, the ζ potential of the membrane surface shifts further away from that of the pristine MoS_2 film, becoming increasingly negative for M-I-Cu membranes and increasingly positive for M-I-C membranes. This trend indicates successful surface functionalization, which significantly alters the surface charge characteristics of the membranes. Cationic CTAB adsorbs onto MoS_2 via hydrophobic interactions, reversing the membrane's surface potential to positive.[50] Interestingly, the presence of Cu NPs on the nanosheets enhances the negative surface charge of the already negatively charged membranes. Moreover, the ζ potential exhibits an abnormal further decrease as the pH drops. Mulliken charge analysis (Figure 3g,h) elucidates the electronic mechanism behind charge modulation. During Cu NP formation, the average charge on Cu drops from 1.11 in $Cu(OAc)_2$ to 0.31 in Cu_2 clusters, with a parabolic correlation (R^2 = 0.914) between the cluster size and charge. This indicates increased charge transfer from Cu to the MoS_2 surface upon aggregation, enhancing the negative surface potential. Conversely, M-I-C increases the average charges of Mo and S sites, whereas M-I-Cu decreases them, directly governing their respective positive and negative surface polarities. This is further corroborated by a continuous upward shift in the Mo 4d band center from M-I-Cu to M-I-C, aligning with the increased positive charge on Mo sites. Such a distinct electronic modulation enables high selectivity for removing oppositely charged nanopollutants.

To evaluate the ability of the modified membranes to promote the agglomeration of nanopollutants, aqueous dispersions of PS nanoparticles (negatively charged) and TiO_2 nanoparticles (positively charged, as confirmed in Figure S19) were employed as model nanopollutants with opposite surface charges. After immersion of the membranes in each dispersion and standing for 10 min, the particle size of the colloidal suspensions was measured. The results in Figure 4a,d demonstrate that the functionalized membrane effectively promotes the aggregation of nanoparticles carrying opposite surface charges, while having no significant effect on those with the same charge. Furthermore, the extent of aggregation increases with the magnitude of the surface charge, as evidenced by the larger aggregate sizes observed. To examine the time-dependent aggregation behavior, time-resolved dynamic light scattering (TR-DLS) was performed (Figure S20). The 3D trajectory profiles explicitly capture a continuous, concentration-dependent particle size escalation across the 0−10 min timeline, directly validating the high-efficiency operational kinetics of the charge-induced aggrega-

https://doi.org/10.1021/acs.nanolett.6c02107
Nano Lett. XXXX, XXX, XXX−XXX

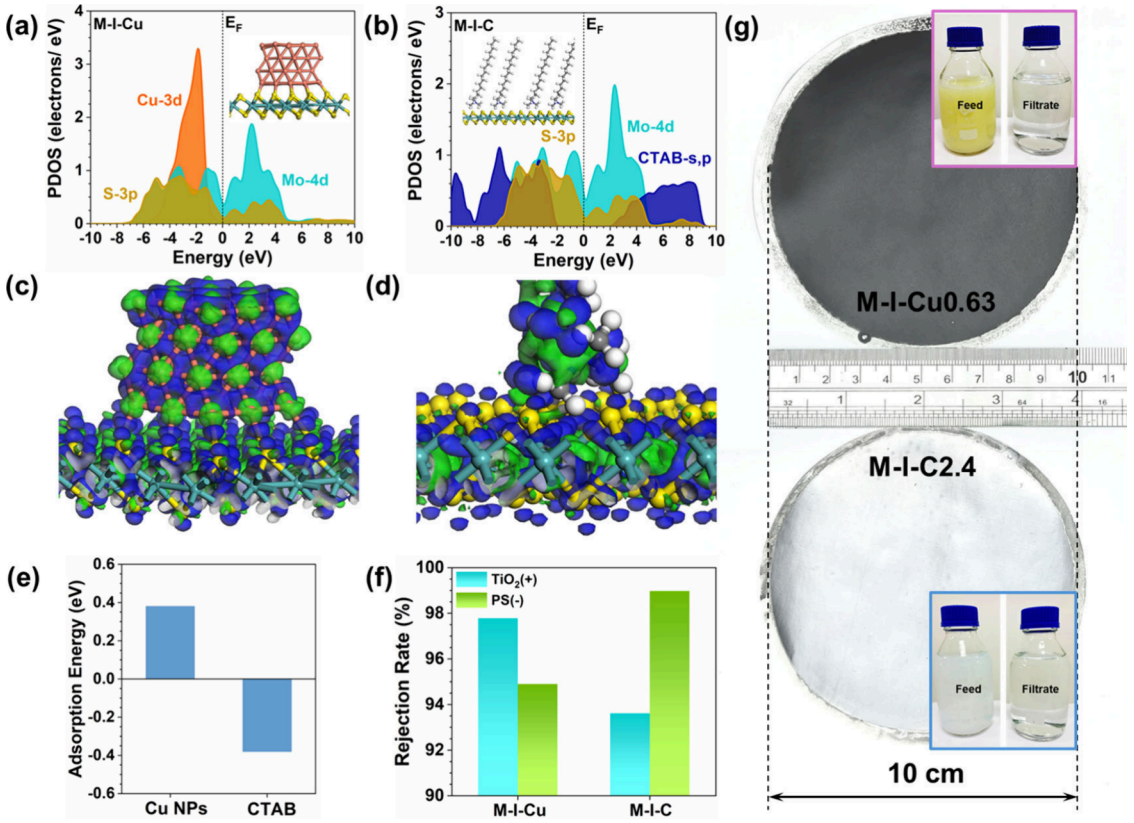

Figure 5. PDOS of (a) M-I-Cu and (b) M-I-C. Insets are the relaxed structures. Balls: orange, Cu; cyan, Mo; yellow, S. Electron density differences of (c) M-I-Cu and (d) M-I-C. Blue isosurface = electron accumulation, and green isosurface = electron depletion. (e) Adsorption energies of Cu NPs and CTAB on MoS_2. (f) Calculated rejection ratios of PS and TiO_2 through M-I-Cu and M-I-C. (g) Digital photographs of M-I-Cu0.63 and M-I-C2.4 membranes up to 10 cm in diameter. The insets above and below are the TiO_2 dispersion feed and M-I-Cu0.63 filtrate and the PS dispersion feed and M-I-C2.4 filtrate, respectively.

tion platform under dynamic environments. The rejection rates of the M-I-Cu and M-I-C membranes for PS(−) and TiO_2(+) dispersions were evaluated (UV spectra with different concentrations are shown in Figure S21). Figure S22 shows that the M-I-CuX membrane exhibits excellent rejection performance for both PS(−) and TiO_2(+) dispersions, although the rejection trends differ significantly between them. For negatively charged PS(−) particles, the rejection rate is primarily governed by size exclusion. Consequently, membranes with higher water permeance (indicating larger pore sizes) show a lower rejection rate (Figure 4b), which aligns with most literature reports. In contrast, positively charged TiO_2(+) nanoparticles experience strong electrostatic attraction to the negatively charged membrane surface, promoting significant particle agglomeration. This process increases the effective particle size, leading to enhanced rejection rate—reaching up to 99.68%—even as the water permeance increases to 804.3 $L/m^2 \cdot h \cdot bar$ (Figure 4c). A similar behavior is observed for the M-I-CX membrane, as displayed in Figures 4e,f and S23; that is, with increasing modification, both the water permeance and rejection rate of oppositely charged PS(−) particles rise simultaneously. Even at a water permeance of 512.9 $L/m^2 \cdot h \cdot bar$, the M-I-C2.4 membrane achieves a high rejection rate of 99.43% for PS(−) dispersion. Subsequently, the cycling stability of the membranes was evaluated by repeatedly rejecting nanopollutants following brief cleaning steps. As shown in Figure 4g,h, both functionalized MoS_2 membranes exhibit excellent stability over 10 cycles when rejecting nanopollutants carrying an opposite charge. In contrast, for pollutants with the same charge, the rejection rate gradually decreases with successive cycles. This difference can be attributed to the distinct behaviors of the pollutants: oppositely charged pollutants tend to agglomerate into larger particles that accumulate near the membrane surface and can be readily removed by rinsing, whereas similarly charged nanopollutants, which remain dispersed and do not agglomerate, are more likely to penetrate and block the membrane pores after repeated filtration cycles. When these water purification performances are compared with other reported 2D inorganic nanosheet membranes (Figure 4i and Table S2), our functionalized MoS_2 membranes exhibit higher rejection rates than most other 2D materials-based membranes.

DFT and molecular dynamics (MD) simulations were performed to elucidate the electronic-level mechanisms of the membrane performance. Projected density of states (PDOS) analysis (Figure 5a,b) confirms the structural stability of M-I-Cu, where Cu 3d orbitals (peak at E_V = −1.84 eV) align well with Mo 3d and S 3p orbitals. For M-I-C, CTAB modification elevates the Mo 4d band center from E_V = −1.11 eV to E_V = −0.65 eV and upshifts S 3p orbitals, increasing the surface valence states. Electron density difference maps (Figure 5c,d) reveal distinct charge-transfer pathways: in M-I-Cu, electrons transfer from Cu to the MoS_2 surface (electron accumulation), whereas in M-I-C, electrons transfer from MoS_2 to CTAB (electron depletion), dictating their respective negative and positive surface potentials. Both modifications exhibit stable adsorption energies (−0.39 eV for Cu and −0.37 eV for

https://doi.org/10.1021/acs.nanolett.6c02107
Nano Lett. XXXX, XXX, XXX−XXX

CTAB). MD simulations (Figures 5f, S24, and S25) corroborate these findings, showing that charge-driven agglomeration dictates selectivity: M-I-Cu achieves higher TiO_2(+) rejection (97.8%), while M-I-C excels in PS(−) removal (99.0%), aligning perfectly with experimental observations.

To establish the operational universality, the rejection performance was examined under a severe ionic strength gradient (Figure S26). Even when the Debye screening length is compressed to ∼0.96 nm under 100 mM NaCl, the membranes securely retain >98.3% of nanopollutants. This outstanding screening resilience is driven by the spatial confinement effect within the subnanometer 2D channels, where the ultrahigh local charge density forces close-range interactions. While baseline steric size exclusion provides a rigorous safeguard, the charge-directed agglomeration breaks the conventional permeability−selectivity trade-off limit. Then, sequential elution leaching tests verify the outstanding chemical stability and environmental safety of this platform for long-term operations; the cumulatively released Cu^{2+} and total organic carbon residuals rapidly decay to negligible background levels within four runs, with the maximum copper leaching concentration (∼0.13 ppm) staying far below the strict regulatory limits required by the World Health Organization (Figure S27). Furthermore, to cross-validate the operational feasibility and delineate the boundary conditions of this technology in mixed-charge environments, a two-step sequential filtration cascade was evaluated using a multicomponent feed stream containing coexisting PS and TiO_2 nanoparticles (Figure S28). By operating complementary M-I-Cu0.63 and M-I-C2.4 membranes as consecutive tandem stages, the system dynamically overcomes the polarity limitation of a single layer, yielding a near-complete macroscale coprecipitation and purification with a stellar combined rejection efficiency of 99.82%. Coupled with large-scale module evaluations [Figure 5g; the membrane area was successfully scaled up to $\pi \times 5^2$ cm^2, and the filtrate remained clear after a single filtration of 500 mL of PS(−) and TiO_2(+) suspensions], these insights confirm that our platform is highly generalizable for complex wastewater treatment through modular configuration.

This study demonstrates a surface-charge-regulated strategy for MoS_2 membranes through functionalization with Cu NPs and CTAB. The M-I-Cu membrane achieves an unprecedented performance in rejecting positively charged TiO_2(+) nanoparticles (99.68%) while maintaining a high water permeance of 804.3 ± 35.4 $L/m^2 \cdot h \cdot bar$. In contrast, the M-I-C membranes effectively remove negatively charged PS(−) nanoparticles (99.43%) at a high water permeance of 512.9 ± 21.1 $L/m^2 \cdot h \cdot bar$. The synergistic combination of 3D porous architecture and charge-selective agglomeration overcomes the intrinsic permeability−selectivity trade-off, providing a scalable platform for high-efficiency nanopollutant removal. Moreover, the charge-directed regulation strategy offers a generalizable approach for designing other 2D membrane materials, with significant potential for advancing future water purification technologies.

■ ASSOCIATED CONTENT

Supporting Information

The Supporting Information is available free of charge at https://pubs.acs.org/doi/10.1021/acs.nanolett.6c02107.

Additional experimental details, materials, and methods, DFT and MD simulation details, TEM, AFM, SEM, XPS, Raman, XRD, ICP, ζ potential, contact angle and water permeance characterizations of pristine and functionalized MoS_2 membranes, structural stability, nanopollutant characterization, time-resolved DLS agglomeration kinetics, UV−vis analyses, MD simulation snapshots, salt tolerance, cycling stability, and cascade filtration performance, comparison of this work with recently reported nanofiltration and 2D material-based membranes in terms of water permeance and nanopollutant rejection (PDF)

■ AUTHOR INFORMATION

Corresponding Authors

Zhiyuan Zeng − *Department of Materials Science and Engineering and State Key Laboratory of Marine Environmental Health, City University of Hong Kong, Hong Kong S.A.R., China;* orcid.org/0000-0001-7483-1438; Email: zhiyzeng@cityu.edu.hk

Bolong Huang − *Department of Chemistry, City University of Hong Kong, Hong Kong S.A.R., China;* orcid.org/0000-0002-2526-2002; Email: b.h@cityu.edu.hk

Authors

Weikang Zheng − *Department of Materials Science and Engineering and State Key Laboratory of Marine Environmental Health, City University of Hong Kong, Hong Kong S.A.R., China*

Qutong Yang − *Department of Materials Science and Engineering and State Key Laboratory of Marine Environmental Health, City University of Hong Kong, Hong Kong S.A.R., China*

Mingzi Sun − *Department of Chemistry, City University of Hong Kong, Hong Kong S.A.R., China*

Honglu Hu − *Department of Materials Science and Engineering and State Key Laboratory of Marine Environmental Health, City University of Hong Kong, Hong Kong S.A.R., China*

Yue Zhang − *Department of Materials Science and Engineering and State Key Laboratory of Marine Environmental Health, City University of Hong Kong, Hong Kong S.A.R., China*

Ruixin Yan − *Department of Materials Science and Engineering and State Key Laboratory of Marine Environmental Health, City University of Hong Kong, Hong Kong S.A.R., China*

Yang Zhou − *Department of Materials Science and Engineering and State Key Laboratory of Marine Environmental Health, City University of Hong Kong, Hong Kong S.A.R., China*

Jingyun Fang − *Guangdong Provincial Key Laboratory of Environmental Pollution Control and Remediation Technology, School of Environmental Science and Engineering, Sun Yat-Sen University, Guangzhou 510275, China;* orcid.org/0000-0001-5997-0384

Alicia Kyoungjin An − *Department of Chemical and Biological Engineering, The Hong Kong University of Science and Technology, Hong Kong S.A.R., China;* orcid.org/0000-0003-0041-2817

Chuyang Y. Tang − *Department of Civil and Environmental Engineering, College of Design and Engineering, National*

University of Singapore, Singapore 117576, Singapore; orcid.org/0000-0002-7932-6462

Zhiguo Yuan − *School of Energy and Environment, City University of Hong Kong, Hong Kong S.A.R., China;* orcid.org/0000-0002-7566-1482

Kenneth M. Y. Leung − *State Key Laboratory of Marine Environmental Health, City University of Hong Kong, Hong Kong S.A.R., China;* orcid.org/0000-0002-2164-4281

Complete contact information is available at: https://pubs.acs.org/10.1021/acs.nanolett.6c02107

Author Contributions

†W.Z., Q.Y., and M.S. contributed equally to this work.

Notes

The authors declare no competing financial interest.

■ ACKNOWLEDGMENTS

Z.Z. gratefully acknowledges financial support from Hong Kong RGC's Young Collaborative Research Grant (No. C1003-23Y) and General Research Fund (No. 11309425), Hong Kong ITC Project ITS/192/23, and City University of Hong Kong's internal grant (Projects 7005462 and 7005623). Z.Z. also acknowledges the Seed Collaborative Research Fund of the State Key Laboratory of Marine Environmental Health (SKLMEH/SCRF/0096), which receives regular research funding from the Innovation and Technology Commission (ITC) of the HKSAR Government (No. 9448002). However, any opinions, findings, conclusions, or recommendations expressed in this publication do not reflect the views of the HKSAR Government or the ITC.

■ REFERENCES

(1) He, L.; Tan, T.; Zeng, B. P.; Gao, Z. X.; Guan, W. Impact of influent quality on the mixed liquor volatile suspended solids/mixed liquor suspended solids of mixed liquor from treatment plant. *Desalination and Water Treatment* **2022**, *280*, 52−59.

(2) Krasavtseva, E. A.; Maksimova, V. V.; Makarov, D.; Masloboev, V. A. Removal of Suspended Solids from Industrial Wastewater. *Journal of Mining Science* **2022**, *58* (3), 466−475.

(3) Larrarte, F. Suspended solids within sewers: an experimental study. *Environmental Fluid Mechanics* **2008**, *8* (3), 249−261.

(4) Selbig, W. R.; Bannerman, R. T. Ratios of Total Suspended Solids to Suspended Sediment Concentrations by Particle Size. *J. Environ. Eng.* **2011**, *137* (11), 1075−1081.

(5) da Costa, J. P.; Santos, P. S. M.; Duarte, A. C.; Rocha-Santos, T. (Nano)plastics in the environment - Sources, fates and effects. *Sci. Total Environ.* **2016**, *566*, 15−26.

(6) Gigault, J.; ter Halle, A.; Baudrimont, M.; Pascal, P. Y.; Gauffre, F.; Phi, T. L.; El Hadri, H.; Grassl, B.; Reynaud, S. Current opinion: What is a nanoplastic? *Environ. Pollut.* **2018**, *235*, 1030−1034.

(7) Peng, L. C.; Fu, D. D.; Qi, H. Y.; Lan, C. Q.; Yu, H. M.; Ge, C. J. Micro- and nano-plastics in marine environment: Source, distribution and threats - A review. *Sci. Total Environ.* **2020**, *698*, No. 134254.

(8) Singh, J.; Dutta, T.; Kim, K. H.; Rawat, M.; Samddar, P.; Kumar, P. Green' synthesis of metals and their oxide nanoparticles: applications for environmental remediation. *J. Nanobiotechnol.* **2018**, *16*, No. 84.

(9) Wang, J.; Wang, J. J.; Liu, Y.; Nie, Y. G.; Si, B.; Wang, T.; Waqas, A.; Zhao, G. P.; Wang, M. M.; Xu, A. Aging-independent and size-dependent genotoxic response induced by titanium dioxide nanoparticles in mammalian cells. *Journal of Environmental Sciences* **2019**, *85*, 94−106.

(10) Mitrano, D. M.; Wick, P.; Nowack, B. Placing nanoplastics in the context of global plastic pollution. *Nat. Nanotechnol.* **2021**, *16* (5), 491−500.

(11) Woodward, J.; Li, J. W.; Rothwell, J.; Hurley, R. Acute riverine microplastic contamination due to avoidable releases of untreated wastewater. *Nature Sustainability* **2021**, *4* (9), 793−802.

(12) El-Sawaf, A. K.; Nassar, A. A.; El Aziz Elfiky, A. A.; Mubarak, M. F. Advanced microcrystalline nanocellulose-based nanofiltration membranes for the efficient treatment of wastewater contaminated with cationic dyes. *Polym. Bull.* **2024**, *81* (14), 12451−12476.

(13) Ragab, A. H.; Gumaah, N. F.; Elfiky, A. A.; Mubarak, M. F. Exploring the sustainable elimination of dye using cellulose nanofibrils- vinyl resin based nanofiltration membranes. *BMC Chem.* **2024**, *18* (1), No. 121.

(14) Singh, V.; Ahmed, G.; Vedika, S.; Kumar, P.; Chaturvedi, S. K.; Rai, S. N.; Vamanu, E.; Kumar, A. Toxic heavy metal ions contamination in water and their sustainable reduction by eco-friendly methods: isotherms, thermodynamics and kinetics study. *Sci. Rep.* **2024**, *14* (1), No. 7595.

(15) Tian, M. T.; Liu, Y.; Zhang, S. Z.; Yu, C.; Ostrikov, K.; Zhang, Z. H. Overcoming the permeability-selectivity challenge in water purification using two-dimensional cobalt-functionalized vermiculite membrane. *Nat. Commun.* **2024**, *15* (1), No. 391.

(16) Saglam, S.; Türk, F. N.; Arslanoglu, H. Use and applications of metal-organic frameworks (MOF) in dye adsorption: Review. *Journal of Environmental Chemical Engineering* **2023**, *11* (5), No. 110568.

(17) Shen, L.; Cheng, R. H.; Yi, M.; Hung, W. S.; Japip, S.; Tian, L.; Zhang, X.; Jiang, S. D.; Li, S.; Wang, Y. Polyamide-based membranes with structural homogeneity for ultrafast molecular sieving. *Nat. Commun.* **2022**, *13* (1), No. 500.

(18) Yang, Y. L.; Yu, L.; Chu, T. C.; Niu, H. Y.; Wang, J.; Cai, Y. Q. Constructing chemical stable 4-carboxyl-quinoline linked covalent organic frameworks via Doebner reaction for nanofiltration. *Nat. Commun.* **2022**, *13* (1), No. 2615.

(19) Avornyo, A.; Chrysikopoulos, C. Applications of graphene oxide (GO) in oily wastewater treatment: Recent developments, challenges, and opportunities. *Journal of Environmental Management* **2024**, *353*, No. 120178.

(20) Sable, H.; Kumar, V.; Singh, V.; Rustagi, S.; Chahal, S.; Chaudhary, V. Strategically engineering advanced nanomaterials for heavy-metal remediation from wastewater. *Coord. Chem. Rev.* **2024**, *518*, No. 216079.

(21) Ding, L.; Li, L. B.; Liu, Y. C.; Wu, Y.; Lu, Z.; Deng, J. J.; Wei, Y. Y.; Caro, J.; Wang, H. H. Effective ion sieving with $Ti_3C_2T_x$ MXene membranes for production of drinking water from seawater. *Nature Sustainability* **2020**, *3* (4), 296−302.

(22) Liu, T.; Liu, X. Y.; Graham, N.; Yu, W. Z.; Sun, K. N. Two-dimensional MXene incorporated graphene oxide composite membrane with enhanced water purification performance. *J. Membr. Sci.* **2020**, *593*, No. 117431.

(23) Hirunpinyopas, W.; Prestat, E.; Worrall, S. D.; Haigh, S. J.; Dryfe, R. A. W.; Bissett, M. A. Desalination and Nanofiltration through Functionalized Laminar MoS_2 Membranes. *ACS Nano* **2017**, *11* (11), 11082−11090.

(24) Wang, Z. Y.; Tu, Q. S.; Zheng, S. X.; Urban, J. J.; Li, S. F.; Mi, B. X. Understanding the Aqueous Stability and Filtration Capability of MoS_2 Membranes. *Nano Lett.* **2017**, *17* (12), 7289−7298.

(25) Mei, L.; Sun, M.; Yang, R.; Ying, T.; Yan, R.; Zheng, W.; Zhang, Y.; Hu, H.; Voiry, D.; Leung, K. M. Y.; et al. High efficiency gold extraction by 2D metallic 1T/1T′ phase transition metal dichalcogenides. *Nat. Commun.* **2026**, DOI: 10.1038/s41467-026-75803-1.

(26) Mei, L.; Sun, M.; Yang, R.; Zhang, Y.; Zhang, Y.; Zhang, Z.; Zheng, L.; Chen, Y.; Zhang, Q.; Zhou, J.; et al. Metallic 1T/1T′ phase TMD nanosheets with enhanced chemisorption sites for ultrahigh-efficiency lead removal. *Nat. Commun.* **2024**, *15* (1), No. 7770.

(27) Li, W. L.; Lin, W. T.; Zhu, C. Y.; Fu, P.; Zhou, D.; Huang, X. J.; Xu, Z. K.; Wan, L. S. High-performance thin film composite nanofiltration membranes with MoS_2 nanosheet interlayer. *J. Membr. Sci.* **2023**, *685*, No. 121956.

(28) Wang, W. S.; Onofrio, N.; Petit, E.; Karamoko, B. A.; Wu, H. L.; Liu, J. F.; Li, J.; Qi, K.; Zhang, Y.; Gervais, C.; et al. High-surface-area functionalized nanolaminated membranes for energy-efficient nanofiltration and desalination in forward osmosis. *Nature Water* **2023**, *1* (2), 187−197.
(29) Zhu, J. Y.; Meng, W. Q.; Xue, Q.; Zhang, K. S. Two dimensional sulfonated molybdenum disulfide (S-MoS_2) thin-film nanocomposite nanofiltration membrane for selective desalination. *J. Membr. Sci.* **2023**, *676*, No. 121574.
(30) Werber, J. R.; Deshmukh, A.; Elimelech, M. The Critical Need for Increased Selectivity, Not Increased Water Permeability, for Desalination Membranes. *Environmental Science & Technology Letters* **2016**, *3* (4), 112−120.
(31) Yang, Z.; Sun, P. F.; Li, X. H.; Gan, B. W.; Wang, L.; Song, X. X.; Park, H. D.; Tang, C. Y. A Critical Review on Thin-Film Nanocomposite Membranes with Interlayered Structure: Mechanisms, Recent Developments, and Environmental Applications. *Environ. Sci. Technol.* **2020**, *54* (24), 15563−15583.
(32) Park, H. B.; Kamcev, J.; Robeson, L. M.; Elimelech, M.; Freeman, B. D. Maximizing the right stuff: The trade-off between membrane permeability and selectivity. *Science* **2017**, *356* (6343), No. eaab0530.
(33) Mei, L.; Gao, Z.; Yang, R.; Zhang, Z.; Sun, M.; Liang, X.; Zhang, Y.; Ying, T.; Hu, H.; Li, D.; et al. Phase-switchable preparation of solution-processable WS_2 mono- or bilayers. *Nature Synthesis* **2025**, *4* (3), 303−313.
(34) Yang, R.; Mei, L.; Lin, Z.; Fan, Y.; Lim, J.; Guo, J.; Liu, Y.; Shin, H. S.; Voiry, D.; Lu, Q.; et al. Intercalation in 2D materials and in situ studies. *Nature Reviews Chemistry* **2024**, *8* (6), 410−432.
(35) Yang, R.; Fan, Y.; Mei, L.; Shin, H. S.; Voiry, D.; Lu, Q.; Li, J.; Zeng, Z. Synthesis of atomically thin sheets by the intercalation-based exfoliation of layered materials. *Nature Synthesis* **2023**, *2* (2), 101−118.
(36) Yang, R.; Mei, L.; Zhang, Q.; Fan, Y.; Shin, H. S.; Voiry, D.; Zeng, Z. High-yield production of mono- or few-layer transition metal dichalcogenide nanosheets by an electrochemical lithium ion intercalation-based exfoliation method. *Nat. Protoc.* **2022**, *17* (2), 358−377.
(37) Ying, T.; Xiong, Y.; Peng, H. R.; Yang, R. J.; Mei, L.; Zhang, Z.; Zheng, W. K.; Yan, R. X.; Zhang, Y.; Hu, H. L.; et al. Achieving Exceptional Volumetric Desalination Capacity Using Compact MoS_2 Nanolaminates. *Adv. Mater.* **2024**, *36* (31), No. 2403385.
(38) Zeng, Z. Y.; Yin, Z. Y.; Huang, X.; Li, H.; He, Q. Y.; Lu, G.; Boey, F.; Zhang, H. Single-Layer Semiconducting Nanosheets: High-Yield Preparation and Device Fabrication. *Angew. Chem., Int. Ed.* **2011**, *50* (47), 11093−11097.
(39) Wang, H. T.; Lu, Z. Y.; Xu, S. C.; Kong, D. S.; Cha, J. J.; Zheng, G. Y.; Hsu, P. C.; Yan, K.; Bradshaw, D.; Prinz, F. B.; et al. Electrochemical tuning of vertically aligned MoS_2 nanofilms and its application in improving hydrogen evolution reaction. *Proc. Natl. Acad. Sci. U.S.A.* **2013**, *110* (49), 19701−19706.
(40) Zhang, Q.; Jiang, J.; Yan, R.; Yang, R.; Wang, X.; Wang, Q.; Zhang, Z.; Zhang, Q.; Yang, Q.; Dong, Q.; et al. Li^+ intercalation chemistry on 2D transition metal dichalcogenides towards phase evolution, scalable production and application. *National Science Review* **2026**, DOI: 10.1093/nsr/nwag165.
(41) Zhang, P.; Zhu, Q. Z.; Soomro, R. A.; He, S. Y.; Sun, N.; Qiao, N.; Xu, B. In Situ Ice Template Approach to Fabricate 3D Flexible MXene Film-Based Electrode for High Performance Supercapacitors. *Adv. Funct. Mater.* **2020**, *30* (47), No. 2000922.
(42) Wan, C.; Li, R.; Wang, J. P.; Cheng, D. G.; Chen, F. Q.; Xu, L. X.; Gao, M. B.; Kang, Y. Q.; Eguchi, M.; Yamauchi, Y. Silica Confinement for Stable and Magnetic Co-Cu Alloy Nanoparticles in Nitrogen-Doped Carbon for Enhanced Hydrogen Evolution. *Angew. Chem., Int. Ed.* **2024**, *63* (24), No. e202404505.
(43) Pandey, A.; Kumari, S.; Goswami, R. N.; Sharma, O. P.; Islavath, N.; Khatri, O. P. 1T/2H-MoS_2 Heterostructure for Lubrication Enhancement and Tribo-Induced Phase Transformation into 2H-MoS_2. *Acs Applied Engineering Materials* **2024**, *2* (5), 1348−1359.
(44) Liu, H. Y.; Wu, R.; Zhang, H. Y.; Ma, M. Microwave Hydrothermal Synthesis of 1T@2H-MoS2 as an Excellent Photocatalyst. *ChemCatChem.* **2020**, *12* (3), 893−902.
(45) Guo, X. W.; Song, E. H.; Zhao, W.; Xu, S. M.; Zhao, W. L.; Lei, Y. J.; Fang, Y. Q.; Liu, J. J.; Huang, F. Q. Charge self-regulation in 1T‴-MoS_2 structure with rich S vacancies for enhanced hydrogen evolution activity. *Nat. Commun.* **2022**, *13*, No. 5954 DOI: 10.1038/s41467-022-33636-8
(46) Duan, Y. Y.; Wang, Y.; Zhang, W. X.; Zhang, J. W.; Ban, C. G.; Yu, D. M.; Zhou, K.; Tang, J. J.; Zhang, X.; Han, X. D.; et al. Simultaneous CO_2 and H_2O Activation via Integrated Cu Single Atom and N Vacancy Dual-Site for Enhanced CO Photo-Production. *Adv. Funct. Mater.* **2023**, *33* (28), No. 2301729.
(47) Ying, T.; Onofrio, N.; Mei, L.; Peng, H. R.; Zhang, Z.; Gu, M.; Ma, C.; Chen, Y.; Zhou, J.; Leung, K. M. Y.; et al. Vacancy Functionalized MoS_2 Nanolaminated Membranes for Efficient Sieving in Forward Osmosis. *Adv. Mater.* **2025**, *37*, No. e04781 DOI: 10.1002/adma.202504781
(48) Mei, L.; Cao, Z. L.; Ying, T.; Yang, R. J.; Peng, H. R.; Wang, G.; Zheng, L.; Chen, Y.; Tang, C. Y.; Voiry, D.; et al. Simultaneous Electrochemical Exfoliation and Covalent Functionalization of MoS_2 Membrane for Ion Sieving. *Adv. Mater.* **2022**, *34*, No. 2201416 DOI: 10.1002/adma.202201416
(49) Zhang, Y.; Sun, M. Z.; Yang, R. J.; Ying, T.; Mei, L.; Yan, R. X.; Zheng, W. K.; Hu, H. L.; An, A. K.; Liu, B. L.; et al. Scalable Production and Covalent Functionalization of WS_2 Nanosheets for Membrane Fabrication and Ion Separation. *Nano Lett.* **2026**, *26* (11), 3768−3775.
(50) Song, G. B.; Fan, W. C.; Zhang, J.; Xue, T. F.; Shi, Y. W.; Sun, Y.; Ding, G. H. Adsorption of anionic dyes from aqueous solutions by a novel CTAB/ MXene/carbon nanotube composite: Characterization, experiments, and theoretical analysis. *Appl. Surf. Sci.* **2024**, *661*, No. 160036.